OXFORD

Human Molecular Genetics, 2022, Vol. 31, 22, 3897–3913
https://doi.org/10.1093/hmg/ddac146
Advance access publication date 29 June 2022
Original Article

Protein misfolding and clearance in the pathogenesis of a new infantile onset ataxia caused by mutations in *PRDX3*

Dolores Martínez-Rubio[1,2], Ángela Rodríguez-Prieto[3], Paula Sancho[1], Carmen Navarro-González[3], Nerea Gorría-Redondo[4], Javier Miquel-Leal[3], Clara Marco-Marín[5], Alison Jenkins[1], Mario Soriano-Navarro[6], Alberto Hernández[7], Belén Pérez-Dueñas[8], Pietro Fazzari[3,†], Sergio Aguilera-Albesa[4,†] and Carmen Espinós[1,2,9,†,*]

[1]Rare Neurodegenerative Diseases Laboratory, Centro de Investigación Príncipe Felipe (CIPF), Valencia 46012, Spain
[2]Joint Unit CIPF-IIS La Fe Rare Diseases, Valencia 46012, Spain
[3]Cortical Circuits in Health and Disease Laboratory, Centro de Investigación Príncipe Felipe (CIPF), Valencia 46012, Spain
[4]Pediatric Neurology Unit, Department of Pediatrics, Complejo Hospitalario de Navarra, Navarrabiomed, Pamplona 31008, Spain
[5]Structural Enzymopathology Unit, Instituto de Biomedicina de Valencia (IBV), Consejo Superior de Investigaciones Científicas (CSIC), CIBER de Enfermedades Raras (CIBERER-ISCIII), Valencia 46010, Spain
[6]Electron Microscopy Core Facility, Centro de Investigación Príncipe Felipe (CIPF), Valencia 46012, Spain
[7]Service of Advanced Light Microscopy, Centro de Investigación Príncipe Felipe (CIPF), Valencia 46012, Spain
[8]Department of Pediatric Neurology, Hospital Universitari Vall d'Hebron, Vall d'Hebron Institut de Recerca, Barcelona 08035, Spain
[9]Biotechnology Department, Faculty of Veterinary and Experimental Sciences, Universidad Católica de Valencia San Vicente Mártir, Valencia 46001, Spain
*To whom correspondence should be addressed at: Rare Neurodegenerative Diseases Laboratory, Centro de Investigación Príncipe Felipe (CIPF), c/Eduardo Primo Yúfera no. 13, 46012 Valencia, Spain. Tel: +34 96 328 9680; Fax: +34 96 328 9701; Email: cespinos@cipf.es

†The last three authors should be regarded as joint last authors.

Abstract

Peroxiredoxin 3 (PRDX3) encodes a mitochondrial antioxidant protein, which is essential for the control of reactive oxygen species homeostasis. So far, *PRDX3* mutations are involved in mild-to-moderate progressive juvenile onset cerebellar ataxia. We aimed to unravel the molecular bases underlying the disease in an infant suffering from cerebellar ataxia that started at 19 months old and presented severe cerebellar atrophy and peripheral neuropathy early in the course of disease. By whole exome sequencing, we identified a novel homozygous mutation, PRDX3 p.D163E, which impaired the mitochondrial ROS defense system. In mouse primary cortical neurons, the exogenous expression of PRDX3 p.D163E was reduced and triggered alterations in neurite morphology and in mitochondria. Mitochondrial computational parameters showed that p.D163E led to serious mitochondrial alterations. In transfected HeLa cells expressing the mutation, mitochondria accumulation was detected by correlative light electron microscopy. Mitochondrial morphology showed severe changes, including extremely damaged outer and inner membranes with a notable cristae disorganization. Moreover, spherical structures compatible with lipid droplets were identified, which can be associated with a generalized response to stress and can be involved in the removal of unfolded proteins. In the patient's fibroblasts, PRDX3 expression was nearly absent. The biochemical analysis suggested that the mutation p.D163E would result in an unstable structure tending to form aggregates that trigger unfolded protein responses via mitochondria and endoplasmic reticulum. Altogether, our findings broaden the clinical spectrum of the recently described *PRDX3*-associated neurodegeneration and provide new insight into the pathological mechanisms underlying this new form of cerebellar ataxia.

Introduction

The brain is especially sensitive to oxidative stress, reactive oxygen species (ROS) and damage because of its high oxygen consumption (1,2). Elevated levels of ROS are a common etiology in various neurodegenerative disorders (3–5). In the mitochondria, the thioredoxin (TXN) and the glutathione (GSH) systems are crucial to maintain the ROS levels and to prevent oxidative damage. The TXN system consists of TXN2, thioredoxin reductase 2, peroxiredoxins 3 (PRDX3) and 5 (PRDX5). Two ultra-rare diseases are associated with deficiencies in this system, caused by loss-of-function mutations in *TXN2* or *PRDX3* (6,7). For both entities, the underlying disease mechanism is associated with increased ROS levels, impaired oxidative stress defense and mitochondrial dysfunction. *PRDX3*-associated neurodegeneration (PRAN) is characterized by a progressive cerebellar ataxia with a median onset of 21 years, together with hyper- and hypokinetic movement disorders and severe cerebellar atrophy (7). Here, we describe a patient carrying the novel

Received: April 4, 2022. **Revised:** June 9, 2022. **Accepted:** June 27, 2022

PRDX3 p.D163E change in homozygosis, who suffered from a new form of infantile-onset cerebellar ataxia associated with a rapidly progressing cerebellar atrophy and peripheral neuropathy that appears early in the course of the pathology. In the patient's fibroblasts, ROS production was increased and proteins implicated in the TXN system showed altered expression levels. The expression of PRDX3 mutant in primary neurons revealed neurite swellings and impaired morphology. By overexpressing PRDX3 p.D163E in HeLa cells, we observed propensity to aggregation of mitochondria, underpinned by mitochondrial computational parameters. This phenotype was substantially stronger as compared to the one observed for previous known clinical mutations, p.D202N and p.A142G (7). Electron microscopy and correlative light electron microscopy (CLEM) demonstrated that mitochondria were strongly damaged including hollow parts that lacked cristae, and revealed the presence of spherical structures compatible with lipid droplets (LDs), in transfected HeLa cells expressing PRDX3 p.D163E. Global mitochondrial disturbances caused by p.D163E supported the most severe clinical picture of our proband. PRDX3 p.D163E produced an unstable protein that resulted in the formation of insoluble aggregates detected by radioimmunoprecipitation assay (RIPA) subjected to proteolytic degradation with the activation of unfolded protein responses (UPRs) via mitochondria as well as endoplasmic reticulum (ER). Overall, our report expands the PRAN phenotypes and provides new insights into the disease mechanisms of this new form of cerebellar ataxia.

Results

The patient presented early onset rapid progression of cerebellar atrophy with peripheral neuropathy

The proband MD-174, after a normal perinatal history, displayed acute onset of gait ataxia at 19 months old. No triggers were ascertained. In less than 2 weeks, a motor cerebellar syndrome was established; the patient presented ataxia during sitting with loss of autonomous ambulation, dysmetria, dysarthria, tremor and abnormal ocular pursuit movements. Standardized extensive investigations did not reveal any abnormalities at that time (8,9). Brain magnetic resonance imaging (MRI) was normal (Fig. 1A and F). Clinical follow-up during the first 4 months after the onset showed consistency with a motor cerebellar syndrome with a chronic course. At 23 months old, MRI revealed a global cerebellar atrophy, with a decrease from 61 to 52% (Fig. 1A, B and L). At 32 months old, clinical course was stable without any additional clinical signs, but cerebellar atrophy progressed (midsagittal vermis relative diameter, MVRD, 42%; Fig. 1C and L) together with the development of cerebellar cortical hyperintensities that suggested neurodegeneration (Fig. 1H) (10,11). At the age of 4, scale for the assessment and rating of ataxia (SARA) was first applied to assess the severity of the disease, obtaining a score of 26/40. Physical examinations did not show any additional clinical signs at that time, but a nerve conduction study (NCS) revealed moderate signs of motor and sensory neuropathy, predominantly in lower limbs; NCS at 19 months old was normal. From 4 to 6.5 years of age, the clinical course was stable with some improvements in postural and action tremor, retaining walking abilities with assistance. SARA total score was 19/40 at both 5 and 6.5 years old. Receptive language, cognitive, affection, social skills and academic achievement evolved normally during the first 5 years after the onset of the disease. On the contrary, brain MRI showed rapid progression of global cerebellar atrophy ascertained by the decrease of MVRD over time, with early onset cerebellar cortical hyperintensities (Fig. 1A–L).

We investigated by whole exome sequencing the proband and his parents. The novel mutation NM_006793.5:c.489C > G (p.D163E) in *PRDX3* was identified in homozygosis in the proband, and in heterozygosis in each progenitor. The further segregation analysis confirmed these findings and showed that his healthy brother was carrier of the *PRDX3* c.489C > G variant in heterozygosis (Fig. 1M). *In silico* analysis predicted that the variant was deleterious according to the American College of Medical Genetics (ACMG) criteria (12), and the residue was located in a conserved region (data not shown).

Antioxidant system is impaired in the patient's fibroblasts

Since PRDX3 is a mitochondrial antioxidant protein (13), we investigated if the patient's fibroblasts were affected by the H_2O_2 concentration. MitoSox™ Red measurements displayed increased mitochondrial superoxide levels in MD-174's fibroblasts as the H_2O_2 concentration increased ($^*P < 0.05$), surpassing the control cell line (Fig. 2A). Most intracellular ROS are derived from mitochondrial superoxide, which is efficiently dismutated to H_2O_2 via superoxide dismutase, making mitochondria a major site for H_2O_2 generation (6,14,15). In MD-174's fibroblasts, an impairment in scavenging H_2O_2 caused by PRDX3 p.D163E could be expected.

We further investigated the viability of the fibroblasts by an *in vitro* 3-(4,5-dimethylthiazol-2-yl)-5-(3-carboxymethoxyphenyl)-2- (4-sulfophenyl)-2H- tetrazolium) (MTS) assay after treatment with H_2O_2, showing that in both cases (control and proband), cell viability was reduced to a higher extent in 100 μM H_2O_2 (Fig. 2B), supporting the importance of PRDX3 for the oxidative stress defense system. We then studied its effect on cell viability after exposition to L-BSO (L-buthionine sulfoximine), a potent inhibitor of GSH synthesis. For both lines, cell viability decreased upon L-BSO increase (Fig. 2C), with the patient's fibroblasts showing higher sensitivity compared to those of a healthy individual ($^*P < 0.05$; $^{**}P < 0.01$).

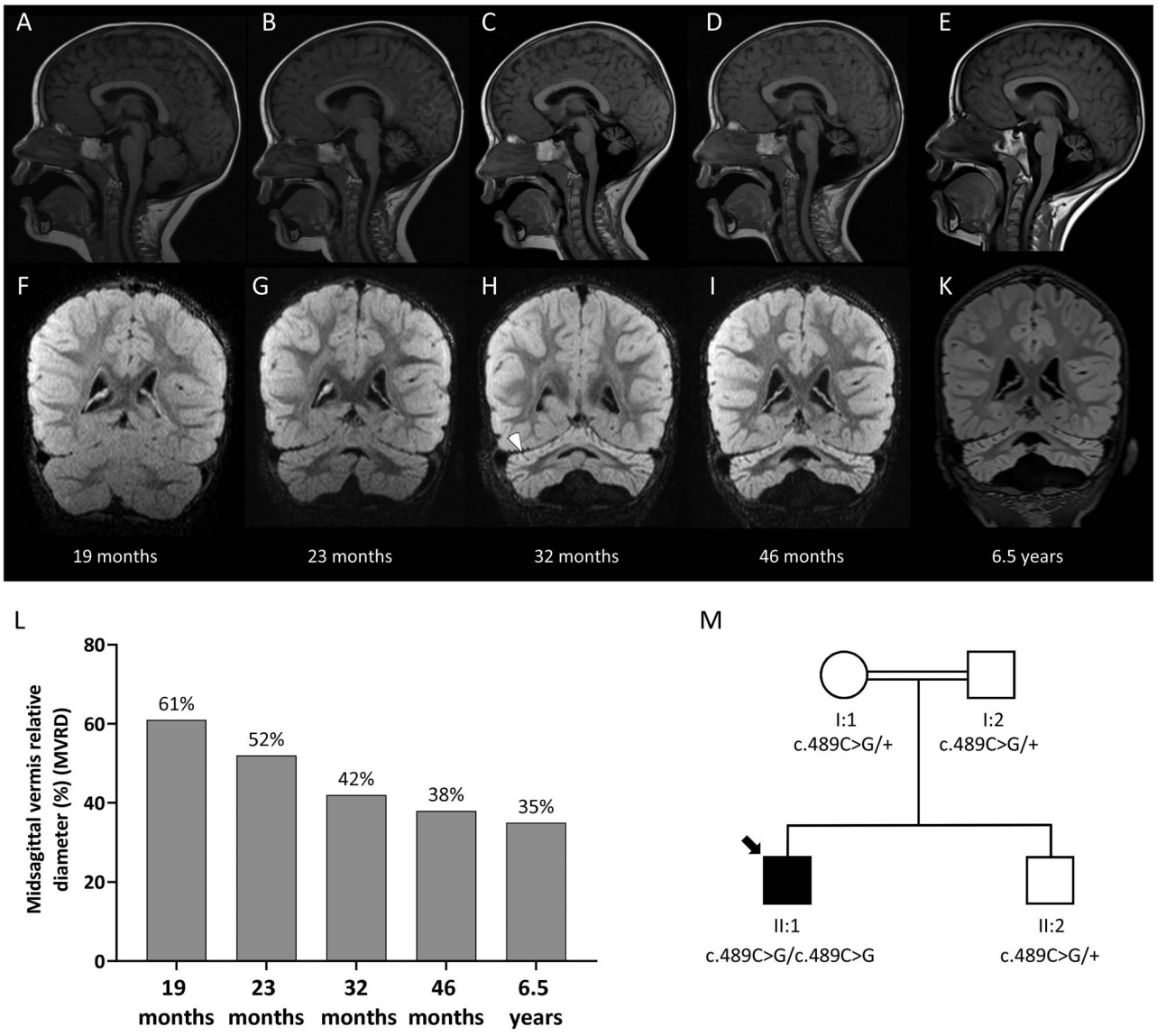

Figure 1. Brain MRI and pedigree of the proband. (**A–F**) Consecutive brain MRI of the patient from onset of ataxia at 19 months to 6.5 years of age. (A–E) Midsagittal T1-weighted images showing vermian atrophy over time. (**F–K**) Coronal FLAIR images revealing atrophy of cerebellar hemispheres and early appearance of cerebellar cortical hyperintensities (red arrow head). (**L**) Quantitative analysis using the midsagittal vermis relative diameter (MVRD). The vermis diameter/total posterior cranial fossa diameter ratio (%) was used to represent the proportion of both values. (**M**) Pedigree of the proband. The arrow indicates the proband MD-174. Mutation segregation *PRDX3* c.489C > G (p.D163E) is below each symbol.

The TXN and the GSH pathways function in parallel to protect mitochondria from oxidative stress (16). We analyzed the mRNAs expression of pivotal genes involved in the antioxidant TXN system. The patient's fibroblasts showed a significantly increased expression of SOD2/manganese superoxide dismutase (MnSOD) (Fig. 2D), which may be caused by a high concentration of superoxide. Interestingly, we observed lower expression of SOD1 mRNA, which shares function with SOD2, suggesting a compensatory or regulatory mechanism, together with increased SOD2 expression (SOD1, SOD2, $^{*}P < 0.05$). H_2O_2 must be removed mainly by glutathione peroxidases (GPXs), PRDXs and catalase. Consistently, GPX1, GPX4, PRDX5, catalase and TXN2 mRNAs displayed a high expression (GPX1, $^{*}P < 0.05$), which may be caused by a dysfunctional PRDX3. Noteworthy, the mRNA level of PRDX3 was not altered in MD-174's cell line, indicating that the synthesis of PRDX3 mRNA is not affected by the p.D163E mutation.

PRDX3 p.D163E expression in neurons

In mouse primary cortical neurons, we investigated both developing neurons, at 5 days *in vitro* (D5), and more mature neurons at D12, after transfecting the neurons at D4 with a construct expressing both green fluorescent protein (GFP) and PRDX (WT, wild-type, or p.D163E) (Fig. 3A and B). While the WT-PRDX3 was expressed both in the soma and along the neurites, PRDX3 p.D163E expression was decreased (Fig. 3C, upper graph) and mainly found in the soma (Fig. 3A and C, bottom graph). WT-PRDX3 and PRDX3 p.D163E were mainly located in mitochondria as revealed by colabeling

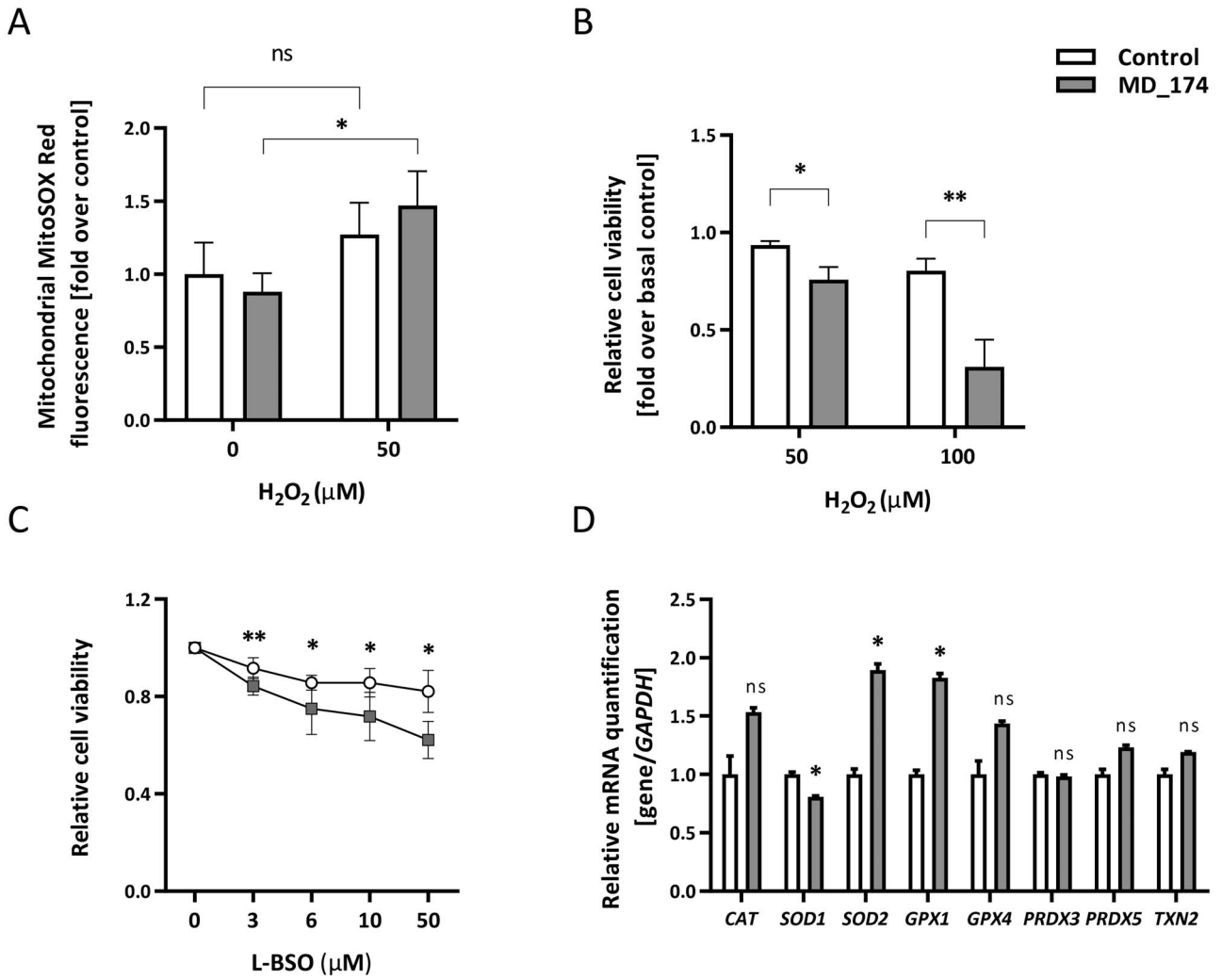

Figure 2. Fibroblasts response to ROS production and related mechanisms. (**A**) Mitochondrial ROS levels were measured using the mitochondrial superoxide indicator MitoSOX Red. (**B**) Fibroblast cell viability studied by MTS Assay under different concentrations of H_2O_2 or (**C**) L-buthionine sulfoximine (L-BSO): optical density (OD) values were normalized to those obtained in basal conditions. (**D**) qPCR-based analysis of targets involved in cellular pathways related to oxidative stress in RNA extracted from both fibroblasts lines. GAPDH was used as the normalizer for the amount of RNA. For both viability assay and qPCR, the measurements obtained for control were set as 1 and the values obtained for the patient were appropriately normalized. Error bars represent SD. *$P < 0.05$; **$P < 0.01$; ns: not significant. Student's test.

with MitoTracker® Red (Fig. 3D). To further investigate the role of the prolonged PRDX3 p.D163E expression in neurons, we examined the morphology of more mature primary cortical neurons at D12 (17,18). Notably, while the morphology of neurons expressing WT-PRDX3 was not distinguishable from control neurons expressing GFP, neurons expressing mutant PRDX3 often displayed different degrees of neurite swelling and impaired morphology (Fig. 3E and F), a hallmark of neuronal degeneration.

PRDX3 mutations elicit severe mitochondrial alterations

PRDX3 is fundamental for maintaining mitochondrial mass, morphology and membrane potential (19). We estimated the distribution of cells according to the mitochondrial morphology in HeLa cells overexpressing PRDX3 WT, p.D163E and reported missense clinical mutations (7). We concluded that p.D163E and p.D202N showed the most impaired patterns, whereas p.A142G's percentages were quite similar to WT (Fig. 4A; Supplementary Material, Fig. S1). In approximately 50% of the cells, mitochondria were aggregated for p.D163E, tubular for p.D202N and intermediate for p.A142G as for WT. To delve in these alterations, we estimated mitochondrial parameters (20). The most remarkable variations were detected for p.D163E: the number of mitochondria as well as the elongation index were decreased, whereas the interconnectivity index was increased (**$P < 0.01$) (Fig. 4B–D). In contrast, p.D202N and p.A142G showed values closer to WT. To better analyze the mitochondrial network, we calculated the mitochondrial branch mean length and the mitochondrial footprint (21). For the mitochondrial branch mean length, the three mutations turned out to be similar to WT, although p.D202N was statistically significant (*$P < 0.05$; Fig. 4E); regarding the mitochondrial footprint, p.D163E was notably reduced (*$P < 0.05$; Fig. 4E). In summary, p.D163E was the

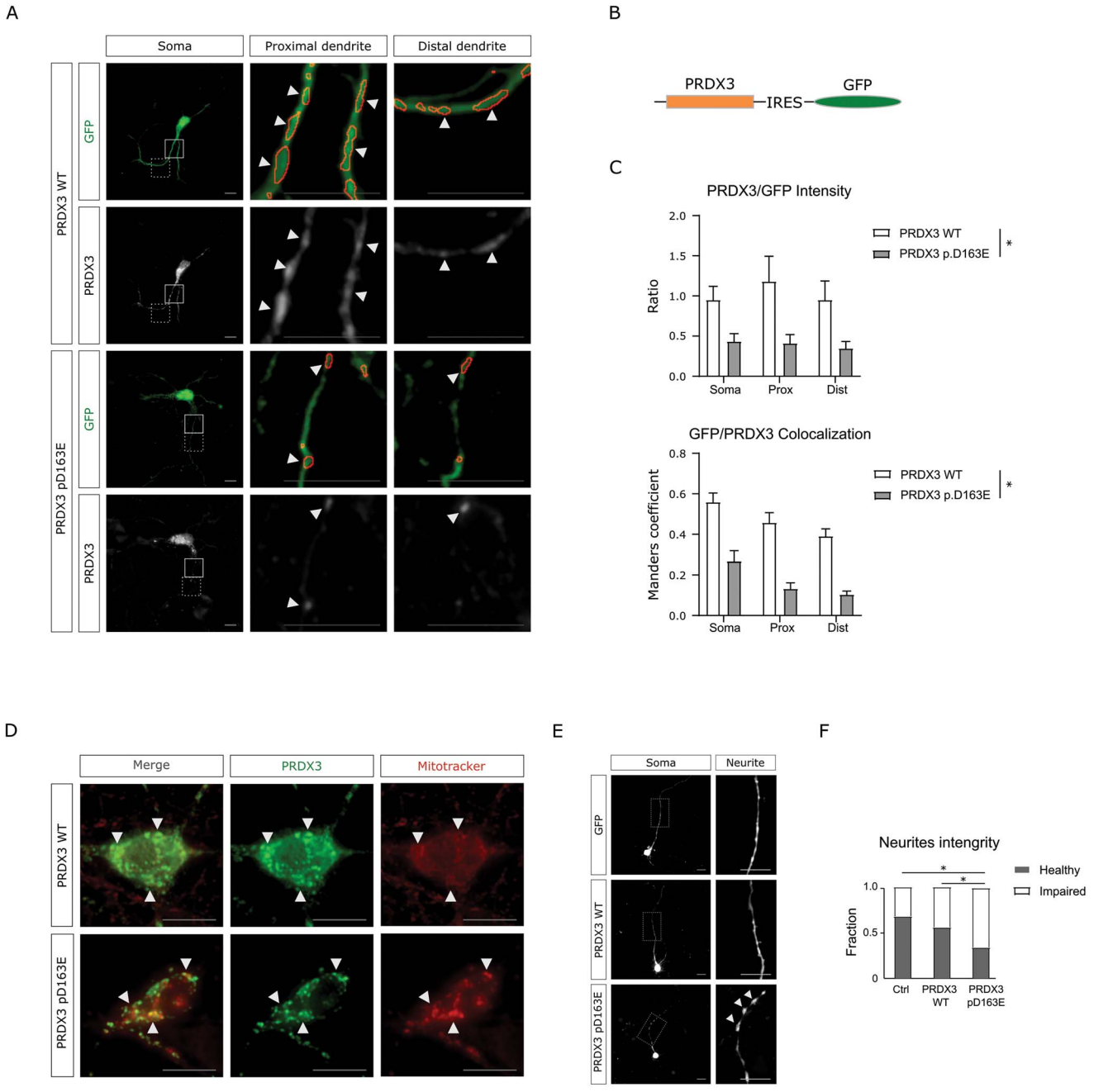

Figure 3. PRDX3 p.D163E expression in primary neurons. (**A**) Representative pictures of primary cortical neurons expressing at D5 either WT-PRDX3 or PRDX3 p.D163E. Boxed area shows the regions magnified and indicated as proximal and distal (solid and dashed lines, respectively). Arrowheads and red lines show the GFP positive regions that colocalized with PRDX3 protein in the neurites. Scale bar = 10 μm. (**B**) Schematic representation of the vector for the co-expression of PRDX3 and GFP linked by an internal ribosome entry site (IRES). (**C**) Upper graphs show either the ratio of the intensity of GFP and PRDX3 labeling. $n = 20$ control or mutant neurons. *$P < 0.05$, two-way ANOVA test. Average ± SEM. Lower graph shows the colocalization expressed as Manders' Overlap Coefficient of PRDX3 over GFP labeling, overlapping areas are lined in red in (A). $n \geq 15$ control or mutant neurons. *$P < 0.05$, two-way ANOVA test. Mean ± SEM. (**D**) Representative pictures of primary neurons at D5 expressing either PRDX3 WT or p.D163E mutant co-labeled with MitoTracker® Red. Full arrowheads indicate regions of co-localization. Scale bar = 10 μm. (**E**) Representative neurons at D12 expressing either PRDX3 WT or PRDX3 p.D163E mutant labeled with GFP. The box indicates the area of the neurite magnified or the right panels. Arrowheads indicate axonal swellings. Scale bar = 10 μm. (**F**) Quantification of neurite integrity based on the neuronal morphology. Ctrl, $n = 50$; PRDX3 WT, $n = 109$; PRDX3 mut, $n = 109$. *$P < 0.05$; Fisher's exact test.

mutation with the most altered mitochondrial parameters. The changes detected in elongation, interconnectivity and mitochondrial footprint revealed that p.D163E caused some tendency to abnormal accumulation. We conclude that mitochondria morphology would be seriously affected by p.D163E, which was consistent with the most severe clinical picture observed in patient MD-174.

To further investigate the mitochondrial morphology, we carried out CLEM in transfected HeLa cells. In cells expressing p.D163E, we observed colocation of PRDX3 (in green) with mitochondria (Fig. 5A and B),

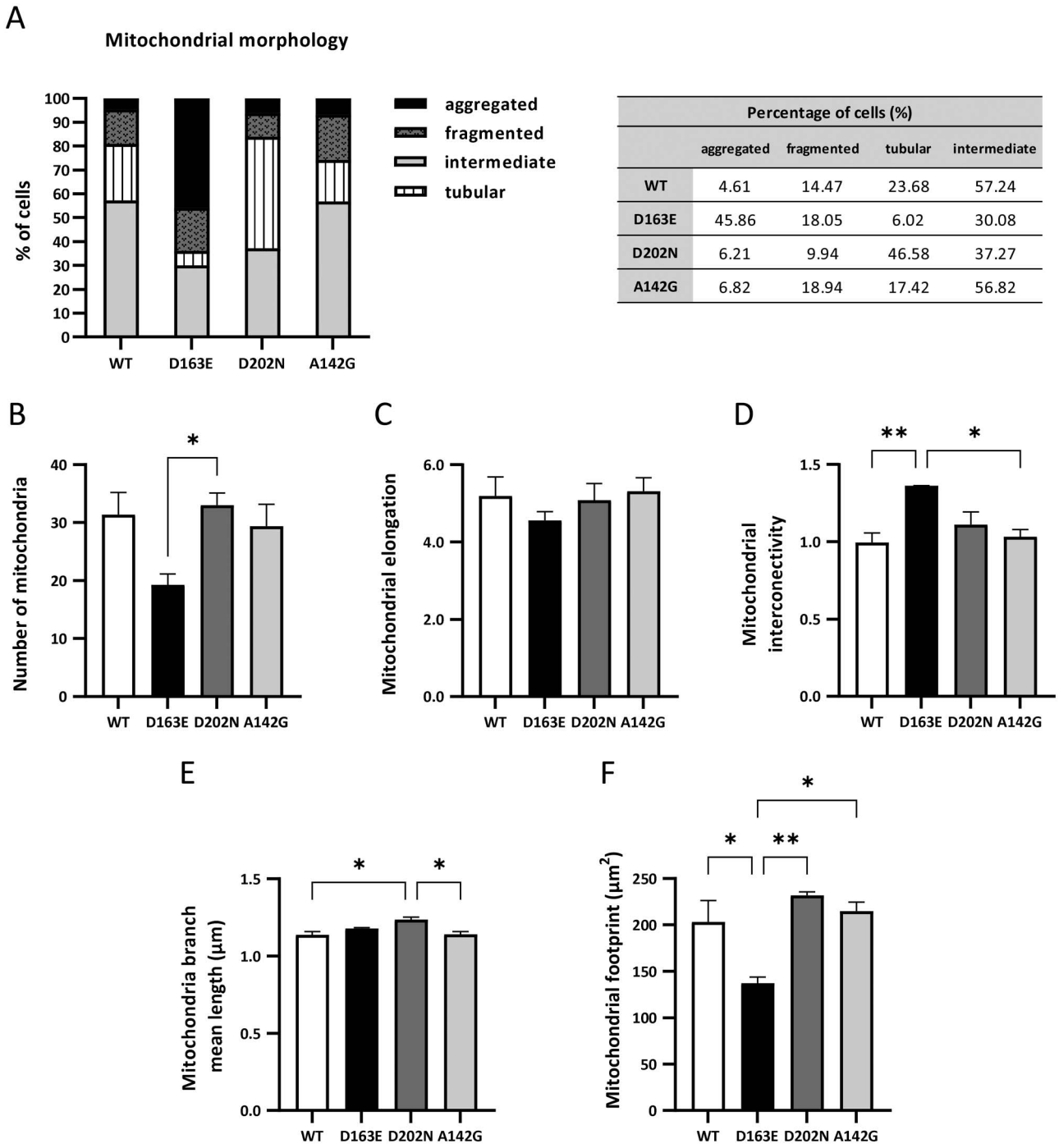

Percentage of cells (%)				
	aggregated	fragmented	tubular	intermediate
WT	4.61	14.47	23.68	57.24
D163E	45.86	18.05	6.02	30.08
D202N	6.21	9.94	46.58	37.27
A142G	6.82	18.94	17.42	56.82

Figure 4. Mitochondrial morphology in HeLa cells overexpressing WT-PRDX3 and mutated forms. (**A**) Distribution of cell percentage according to mitochondrial morphology and obtained percentages for WT and each mutation. (**B–E**) Quantitative analysis of mitochondrial network morphology by the ImageJ™ Mito-Morphology macro. Quantification of the number of mitochondria (B), and the elongation and interconnectivity indices (C, D). (**E, F**) Quantitative analysis of mitochondrial network morphology by the ImageJ™ plugin MiNA. Mean Branch Length is the average of the lengths of all lines used to represent the mitochondrial structures, and the footprint is the total area in the cell occupied by mitochondrial structures. Only statically significant comparatives are shown. Error bars represent SEM. *$P < 0.05$; **$P < 0.01$. One-way ANOVA and Tukey *post hoc* test.

which occasionally were accumulated (Fig. 5C and D). By electron microscopy, we detect that these mitochondria are extremely impaired (Fig. 5E–H) compared to control cells (Fig. 5I–L). In addition to an aberrant morphology, a decrease in cristae was appreciated and even, hollow parts that lacked cristae. What was most striking was the presence of spherical bodies within/near the mitochondria that were absent in the control cells (Fig. 5F–H), suggesting that they are caused by the pathological process. In appearance and density, the spherical forms appeared to be LDs.

The PRDX3 p.D163E mutation produces an unstable protein

Immunostaining and western blot (WB) using an anti-PRDX3 antibody revealed that the PRDX3 p.D163E

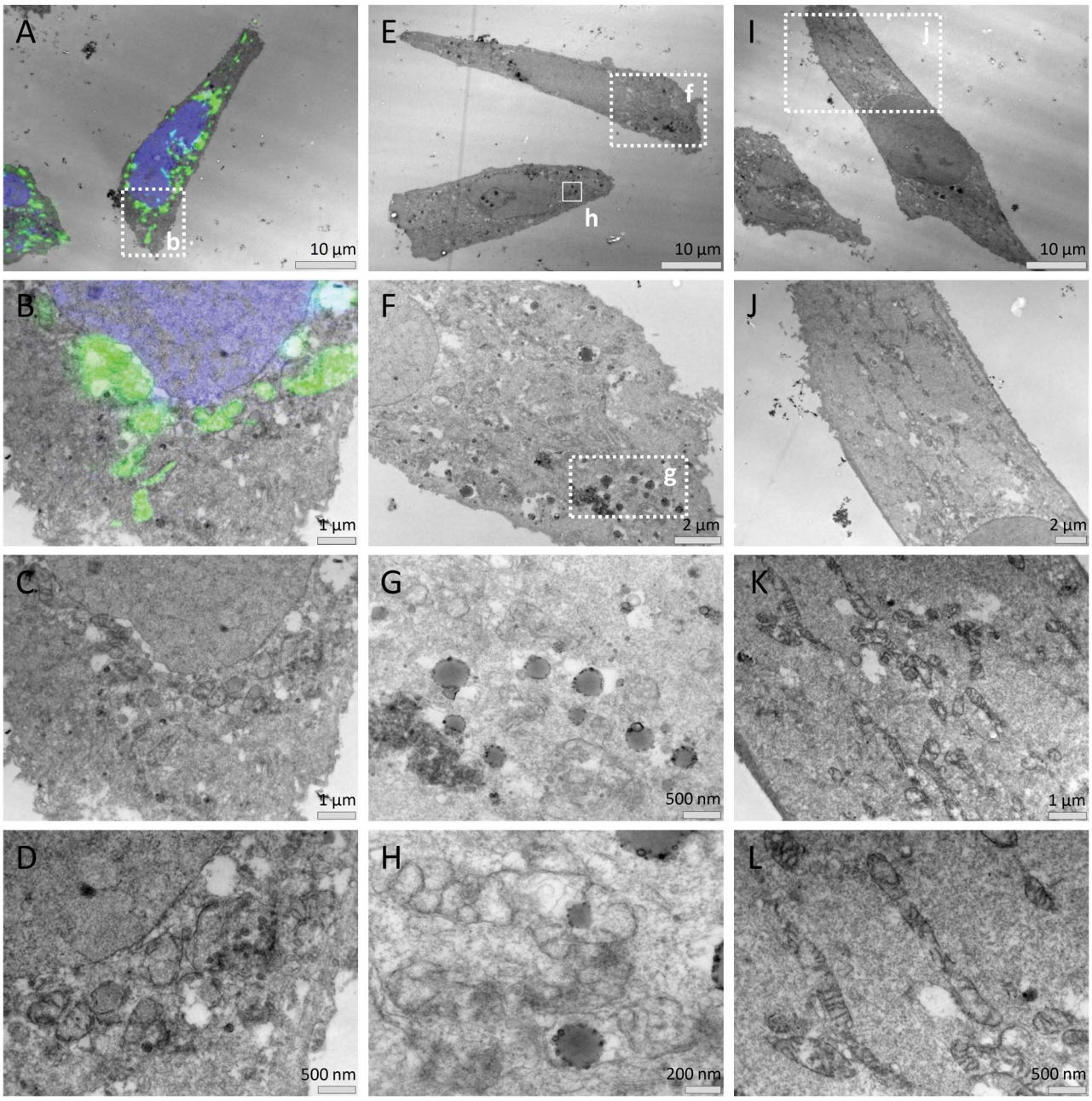

Figure 5. Electron microscopy in transfected HeLa cells expressing PRDX3 p.D163E. HeLa cells were transiently transfected with plasmid DNA encoding PRDX3 p.D163E fused to Myc-DDK tag, immunostained and further processed for transmission electron microscopy (TEM) analysis. (**A**) Correlative light and electron microscopy (CLEM) to identify transfected cells and highlight the localization of the mutated protein (green fluorescence). (**B**) Enlarged picture of the square marked in (A), showing an overlay of p.D163E fluorescence signal and perinuclear clumped mitochondria at the ultrastructural level, observed in more detail in lower panels (**C, D**). Two additional analyzed transfected cells (**E**) and representative TEM high-magnification images (**F–H**) of the boxed regions in (E) displaying aberrant mitochondrial morphology and lipid droplets (LDs) absent in control cells. (**I**) Control non-transfected HeLa cells and successive higher resolution views (**J–L**) of the selected region in (I).

expression was strongly reduced or even absent in the patient's fibroblasts (Fig. 6A and B). PRDX3 is organized in dimers that associate to form dodecamers, which stack to form higher tubular–shaped quaternary organizations (Fig. 6C) (22). It should be noted that D163 is located in a loop that is part of the interface between adjacent subunits in the dodecamer, nearby the catalytic site, where the peroxidatic cysteine is located (Fig. 6D and E). The residue D163 stabilizes an α-helix dipole. Changing to glutamate, although not changing the acidic nature of the side chain, implies an enlargement, which is difficult to accommodate without disturbing the surrounding elements. Given the proximity to the intersubunit surface, p.D163E may lead to destabilization of the oligomer and consequently of the active center, causing loss of function.

In addition, according to the *in silico* prediction made using AGGRESCAN (23), the p.D163E mutation might produce an unstable protein with an increased aggregation tendency of PRDX3 at residues 155–165.

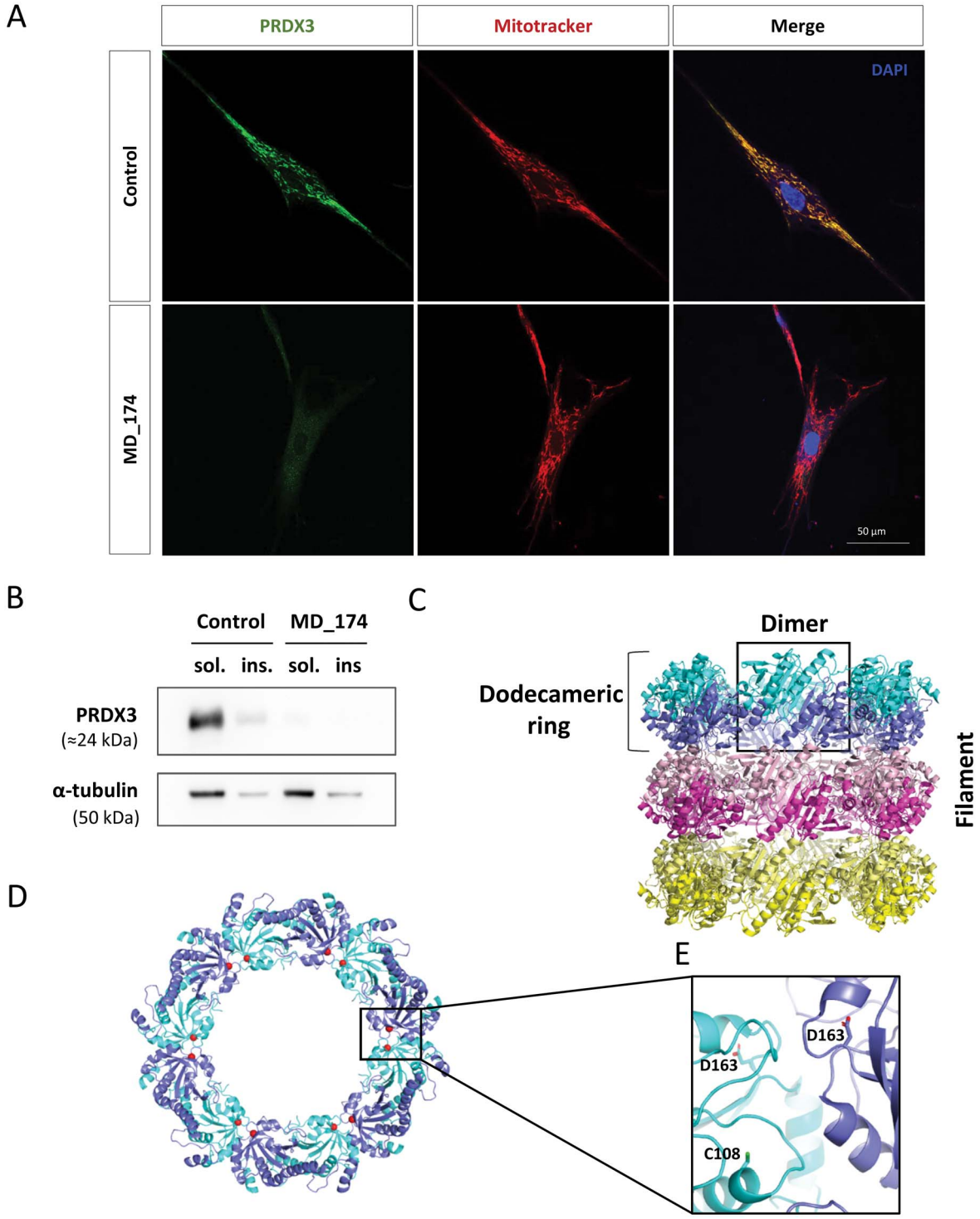

Figure 6. PRDX3 p.D163E expression in fibroblasts and structural analysis. (**A**, **B**) PRDX3 expression in fibroblasts cultures derived from a healthy control and the patient (MD-174). (A) Immunofluorescence showing the subcellular location of WT-PRDX3 and PRDX3 p.D163E (green), the mitochondrial network with MitoTracker® Red and DAPI (blue). Scale bar = 50 μm. (B) WB analysis of the WT and mutated PRDX3 expression in both soluble and insoluble fractions. α-Tubulin was used to normalize the detected protein levels. (**C**) Filament organization of human PRDX3 observed in the crystal structure (PDB ID 5JCG). The subunits of each one of the stacked dodecamers are shown in different colors with different intensities for adjacent subunits. (**D**) Structural model of human ring-like PRDX3 dodecamer. The two subunits of each dimer are colored in light or dark blue, respectively. Localization of D163 is mapped with red spheres. (**E**) Detail of the intersubunit interface, where D163 is located. The side chain of D163 as well as that for the catalytic cysteine 47 is shown with stick representation and labeled.

We calculated the $\Delta\Delta G$ using FoldX (24,25), and the most unstable protein was p.D163E ($\Delta\Delta G = 87.13$ kcal/mol) with much difference compared to the other known missense mutations (7), which revealed protein instability as well (p.D202N, $\Delta\Delta G = 2.70$ kcal/mol; p.A142G, $\Delta\Delta G = 10.49$ kcal/mol). Overall, prediction findings supported that the causative variants, especially p.D163E, enhanced the instability of the PRDX3 protein.

The PRDX3 p.D163E mutation leads to aggregates degraded by the proteasome system

Based on the *in silico* data, we examined the biochemical solubility of WT and mutants (p.D163E, p.D202N and p.A142G) expressed in HeLa cells. The protein carrying p.D163E was absent in the RIPA-soluble fraction (**$P < 0.01$), whereas p.D202N and p.A142G were found in both fractions with a remarkable presence of p.D202N in the insoluble fraction (Fig. 7A–C). On the whole, the three missense clinical mutations seemed to have different behaviors, likely depending on the mutation type and the final conformational consequences. The insoluble fraction can be enriched with unfolded proteins, and therefore p.D163E, and to a lesser extent p.D202N, would produce unfolded proteins.

Unfolded or unstable proteins trigger proteolytic mechanisms. To explore whether p.D163E PRDX3 underwent a degradation process, transfected HeLa cells expressing either the WT or the mutant protein were treated with inhibitors of the ubiquitin proteasome system (UPS) or the autophagy-lysosome pathway. After the proteasome inhibitor treatment (MG-132), a faint band was detected for p.D163E PRDX3, indicating that PRDX3 clearance was due in part to degradation by the proteasome system; nonetheless, after inhibiting autophagy by bafilomycin, no appreciable changes were observed (Fig. 7D). In conclusion, the UPS plays a crucial role in the removal of the mutated protein, which is nearly absent in the patient's fibroblasts.

PRDX p.D163E activates unfolded protein responses

UPRs act together with cell stress signals and proteolytic mechanisms such as the autophagy-lysosome pathway and the UPS (26). The accumulation of damaged or unfolded proteins triggers the UPRs in the ER (UPR^{ER}) and in the mitochondria (UPR^{mt}) to promote homeostasis and to increase proteostasis (26,27). ER load is limited to the upregulation of a handful of gene products, including BiP/HSPA5, its cofactors SDF2L1 and ERj3/DNAJB11, the oxidoreductase ERp72/PDIA4 and HERPUD1 (28). For all these reporters, the expression levels in the patient's fibroblasts were increased in a statistically significant way (*$P < 0.05$) for SDF2L1 and DNAJB11 (Fig. 8A). The UPR^{mt}-mediated protection includes the activation of LONP1, ATF5, HSP60/HSPD1 and PITRM1 (29,30). Statistically significant increased expression levels for LONP1 and ATF5 (*$P < 0.05$; Fig. 8B) were found in the patient's fibroblasts. Similar results were obtained for the ubiquitin ligase MITOL/MARCH5 (*$P < 0.05$; Fig. 8B), located on the junctions between mitochondria and ER, which regulates cellular signaling from mitochondria and from the ER (31). In conclusion, both UPR pathways, in the ER and in the mitochondria, may activate in sync to correct aberrations caused under stress conditions.

Discussion

Neuronal cells consume a large amount of oxygen to maintain their proper function, so they are especially sensitive to deficiencies in the antioxidative defense system of the mitochondria. Defects on TXN2 or PRDX3 trigger a burst of ROS, and both deficiencies drive to early-onset neurodegenerative disorders with severe cerebellar atrophy (6,7). TXN2 deficiency described in one infant was related to a severe psychomotor delay developed early after birth, followed by a spastic-dystonic movement disorder, drug-resistant epilepsy, optic and peripheral neuropathy and resembling classical mitochondrial disorders (6). Conversely, the PRDX3 deficiency was characterized by a mild-to-moderate progressive cerebellar ataxia with onset at a median of 21 years (range 13–22 years), and without any other features of classical mitochondrial diseases (7). In both conditions, a severe cerebellar atrophy was established. Our proband showed an infantile-onset cerebellar ataxia, a motor and sensory neuropathy, and a severe cerebellar atrophy with rapid progression after onset of motor cerebellar syndrome, prospectively followed from 19 months to 6 years of age. The progression of cerebellar atrophy was ascertained by a quantitative analysis using MVRD, a 2D analysis that showed a good correlation with cerebellar volume loss over time in other infantile-onset ataxias with cerebellar atrophy (32). In addition, cerebellar cortical hyperintensities were present in coronal FLAIR (fluid-attenuated inversion recovery) images early in the course of the disease, a common neuroimaging finding in other infantile-onset ataxias with neurodegeneration, but also in non-progressive congenital ataxias (10,11). On the contrary, the motor cerebellar syndrome severity, as measured by SARA, showed a mild improvement over time. Thus, this enhancement may be explained by the fact that fine and gross motor functions change significantly in pediatric age during normal development, especially during the first 5 years of age, as suggested in other infantile neurodegenerative phenotypes like phosphomannomutase-2 deficiency (32,33). Altogether, these data broaden the clinical spectrum of disorders associated with defects in the mitochondrial antioxidant TXN system, and specifically in the *PRDX3* gene.

Mitochondrial dysfunction is well established as a hallmark of neurodegeneration. PRDX3 plays a major role in H_2O_2 detoxification and has protective effects in neurons, which are especially sensitive to oxidative stress (34). In mitochondria, superoxide is converted into peroxide by SOD2/MnSOD and ensures that the concentration of H_2O_2 is very low. Superoxide can be decomposed by GPXs, PRDX3 and PRDX5. In the MD-174's fibroblasts, ROS production was higher, and cell viability significantly decreased upon H_2O_2 or L-BSO treatments. Mitochondrial oxidative stress can cause the upregulation of antioxidants such as SODs, GPXs and PRDXs (13). An altered expression of antioxidant enzymes related to the modulation of ROS homeostasis was observed in the

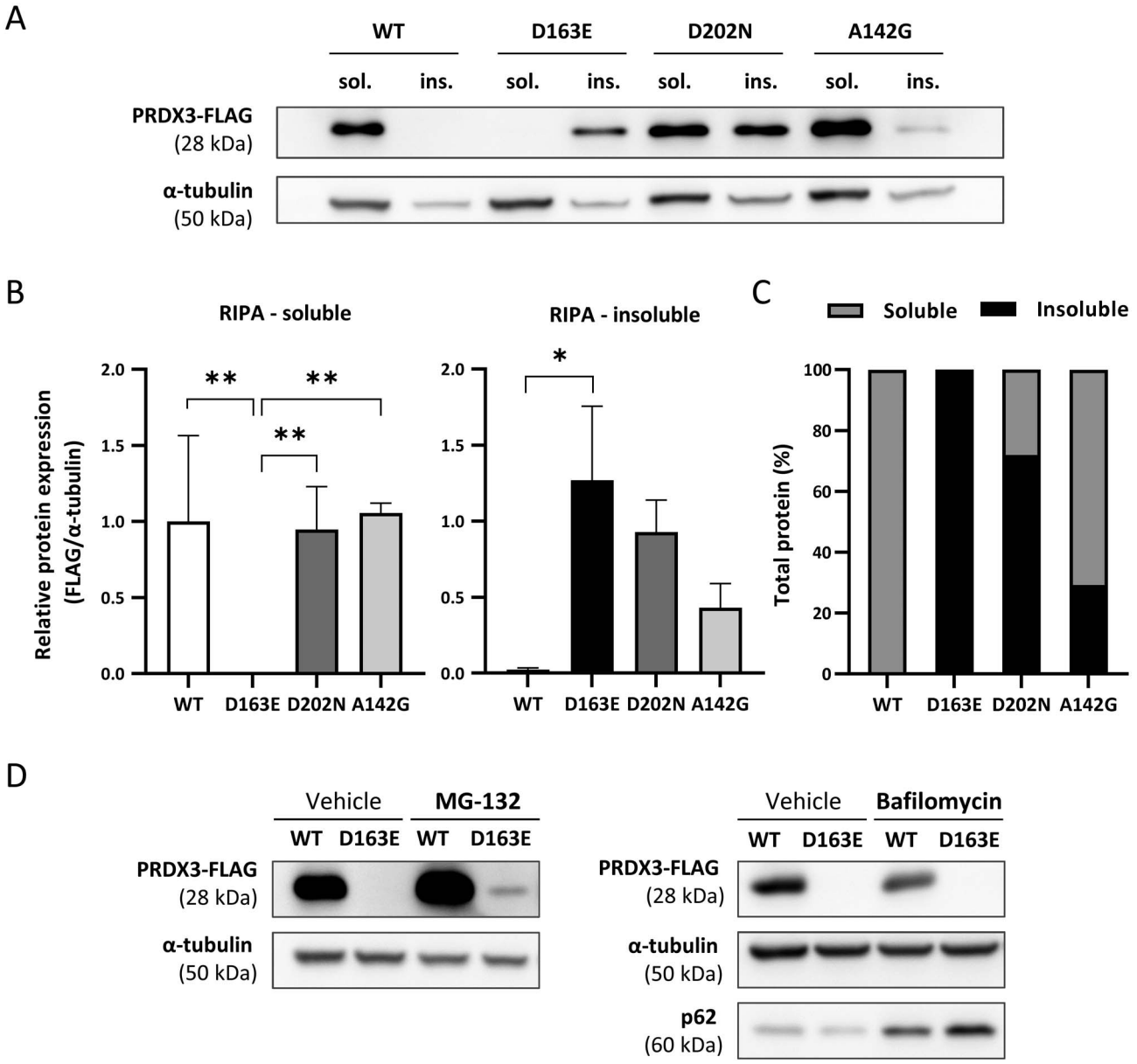

Figure 7. Overexpression of mutated forms of PRDX3 in HeLa cells. (**A**) WB analysis of PRDX3 expression in transfected Hela cells with plasmids expressing WT PRDX3 and mutants. α-Tubulin was used as loading control. (**B**) Densitometric quantification of proteins detected by WB. Error bars represent SEM. *P < 0.05, **P < 0.01, one-way ANOVA followed by Dunnett's test compared to WT. (**C**) Protein levels were normalized to calculate relative presence in both fractions for WT and mutated PRDX3 proteins. (**D**) WB analysis from transfected HeLa cells treated with MG-132 (proteasome inhibitor) or bafilomycin (autophagic inhibitor). The autophagic substrate p62 was used as a bafilomycin control and α-tubulin as loading control.

patient's fibroblasts, which may be a consequence of the cross talk between the mitochondrial TXN and GSH systems in a coregulatory process (16).

The expression of PRDX3 p.D163E in primary cortical neurons was mainly reduced to soma. Mitochondria are primarily produced in the soma, but they must travel long distances to the synaptic terminal (35). When the transport machinery does not work, the neuron results are impaired. MitoTracker® Red labeling was especially intense and the morphology of the neurites was impaired in neurons expressing PRDX3 p.D163E, showing different degrees of neurite alterations. This sign of neuronal stress is prodromal to neuronal degeneration in different neuropathologies and is induced by neurotoxic factors including ROS and excitotoxicity (36–39).

Neurons are particularly sensitive to perturbations in mitochondrial dynamics and we found that *PRDX3* mutations elicit severe alterations in mitochondrial morphology. Compared to WT, p.D202N and p.A142G had no remarkable differences. However, p.D202N presented an increased mitochondrial branch mean length, which likely reflects the associated tubular pattern. p.D163E showed a high value of interconnectivity and a slight reduction of elongation together with a decreased number of mitochondria. Higher scores for interconnectivity signify that mitochondria have more physical connections (40). This finding was additionally reinforced

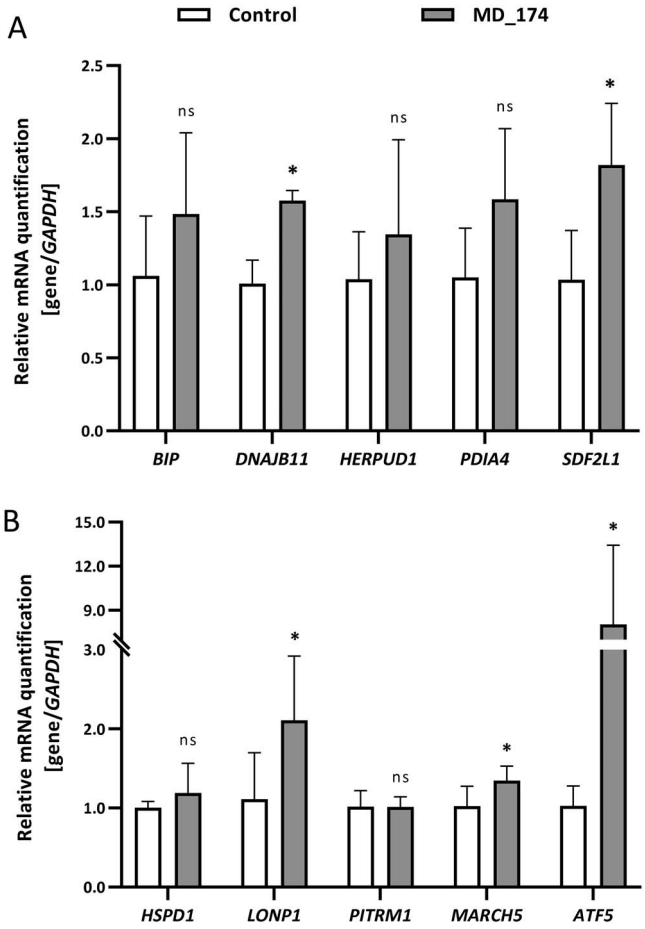

Figure 8. Analysis of the unfolded protein response (UPR). In RNA extracted from fibroblasts of control and patient, qPCR (quantitative PCR)-based analysis of genes related to the endoplasmic reticulum (**B**) or the mitochondrial (**C**) UPR: GAPDH was used as the normalizer for the amount of RNA. The measurements obtained for the control were set as 1 and the values obtained for the patient were appropriately normalized. Error bars represent SD. *$P < 0.05$; **$P < 0.01$; ns: not significant. Student's test.

by the reduced footprint. Taken together, the changes in the mitochondrial morphology indicated severe damages in mitochondria, more than those caused by other *PRDX3* clinical missense mutations, supporting the most severe PRAN phenotype suffered by our proband. In fact, in transfected HeLa cells expressing the PRDX3 p.D163E mutation, electron microscopy revealed that mitochondria were extremely impaired, with abnormal membranes structures, to the extent that they showed little or no cristae. What was surprising was the discovery of spherical structures that resemble LD, near or within mitochondria, which is difficult to establish given the poor state of mitochondria. LDs usually arise from the ER, although they could have an intramitochondrial formation (41). Mitochondrial dysfunction induces formation of LDs as a generalized response to stress, including oxidative stress, and they are involved in the disease mechanism of many neurodegenerative disorders (42). LDs interact with many cellular organelles including mitochondria, and supply lipids as well as unfolded and harmful proteins to LDs, thus assisting in the removal of protein aggregates when severe proteotoxic stress overwhelms the proteasomal system (43,44). According to the findings obtained for the PRDX3 p.D163E protein, which tends to form aggregates of unfolded proteins, it is reasonable to assume that LDs help in the clearance of these mutated proteins.

PRDX3 was absent in fibroblasts from proband MD-174, like in others previously reported to harbor loss-of-function variants that would generate unstable proteins (7). PRDX3 dimers form dodecamers that are stacked, resulting in filaments with an elusive physiological role, although it is known that PRDX3 dimeric variants have lower peroxidase activity than those forming dodecamers (22,45). p.D163E and the reported p.D202N (7) are proximal to the intersubunit surface, may affect the active center and are predicted to affect complex assembly. Moreover, using computational approaches (AGGRESCAN and FoLDX) (23–25), an aggregation tendency that is usually found in unstable proteins was predicted in the PRDX3 p.D163E protein, and in fact, it was foreseen as a protein with a high instability. The PRDX3 p.D163E protein was only recovered in the detergent-insoluble fraction when expressed in cells, in sharp contrast to WT-PRDX3. The two previously reported missense mutations in PRDX3 were also included in this study (7), and we concluded that the protein that appeared to be the most insoluble was the one that contained the p.D163E mutation, followed by p.D202N and finally, by p.A142G. All in all, findings pointed toward the fact that protein aggregates due to *PRDX3* mutations were not a common feature shared for all mutations and hence different disease mechanisms underlie PRAN.

The accumulation of unfolded proteins generated under stress conditions triggers the UPRs that interact with organelles, including mitochondria, and with cell stress signals and the proteasomal and autophagic systems (26). We established that the p.D163E mutation is degraded via the UPS as already described for p.D202N (7). The analysis of expression of modulators involved in UPR^{mt} and UPR^{ER} allowed us to conclude that both pathways were activated in the patient's fibroblasts. ATF5, LONP1 and MARCH5 play a key role in neuroprotection against mitochondrial and ER stresses, (31,46,47). Their increased expression levels in the patient's fibroblasts pointed toward them being possible new therapeutic targets. In fact, approaches involving UPR activation and ER/mitochondrial stress are emerging for very different disorders, mainly to combat the ill-effects of aging and neurodegeneration (26,48).

Overall, these data suggest that PRDX3 p.D163E produces unstable proteins prone to aggregation, which are removal by the UPS, activating UPRs, but also probably helped by LDs. The almost total absence of PRDX3, a key mitochondrial protein in the antioxidant TXN system, causes oxidative damage and severe alterations in mitochondria, leading to a new form of infantile-onset cerebellar ataxia. This work expands the PRAN

phenotypes and brings new insight into the underlying physiopathology, which improves the diagnosis of these ultra-rare, devastating diseases and provides clues for potential therapeutic interventions.

Materials and Methods

Ethics statement. The studies performed were approved by the Institutional Board Ethics Committee of Hospital Universitari i Politècnic La Fe (Valencia), through the Joint Unit CIPF-IIS La Fe (ref. 2019/0052), and written informed consent was signed by the proband's parents.

Patient in-depth phenotyping

The proband MD-174 is a boy born to healthy consanguineous parents from Morocco. Disease progression data were prospectively collected from onset at 19 months to current 6.5 years of age. Phenotyping included standardized assessments of ataxia and other neurological symptoms, NCS, electromyogram, somatosensory, auditorily and visually evoked potentials and 1.5- and 3-T brain MRI investigations. To assess the progression of cerebellar atrophy, a quantitative analysis using the MVRD was performed in every cerebral MRI. The vermis diameter/total posterior cranial fossa diameter ratio was used to represent the proportion of both values (10,11). Disease severity was assessed by the SARA from 4 years of age (49).

Genetic and *in silico* analyses

The patient was first investigated using the custom panel MovDisord (50). Then, the patient's and his parents' exomes were sequenced. Library construction, exome enrichment, sequencing and primary data analysis were performed at Centre Nacional d'Anàlisi Genòmica (CNAG, Barcelona, Spain). Nimblegen SeqCap EZ MedExome 47 Mb Kit was used for exome enrichment, and libraries were sequenced on a HiSeq with v.4 chemistry 100 bp paired-end reads (Illumina, San Diego, CA, USA).

Bioinformatics analysis was performed as previously described (51). In addition, copy number variation analysis with DEcON v2.0.1 tool using default parameters was conducted (52). Conservation of the residues was investigated using the Clustal Omega tool. Sanger sequencing on an ABI Prism 3130XL analyzer (Applied Biosystems, Foster City, CA, USA) was performed for validation and segregation analysis. Finally, AGGRESCAN was used to predict the aggregation properties of the mutant protein (23), and FoldX to calculate the variation in free energy of the mutations where $\Delta\Delta G$ (energy of the mutation) increases if there is the destabilization of structure upon mutation (24,25).

The dodecameric structure of PRDX3 was built from the crystal structure of this protein (PDB 5UCX) using protein interfaces, surfaces and assemblies using PISA (protein, interfaces, surfaces and assemblies) server at the European Bioinformatics Institute (http://www.ebi.ac.uk/pdbe/prot_int/pistart.html) (53). Filaments formed by stacking of dodecamers were built using crystallographic symmetry. Figures were prepared using PYMOL Molecular Graphics System, v2.0 Schrödinger, LLC (https://pymol.org).

Cell culture

HeLa cells were grown in complete Gibco® Dulbecco's modified eagle medium (DMEM) high-glucose medium supplemented with 10% heat-inactivated fetal bovine serum, 1% penicillin/streptomycin and 1% L-glutamine (Sigma-Aldrich, St. Louis, MO, USA). For skin-cultured fibroblasts, we added 100 μg/ml of normocin™ (InvivoGen, Toulouse, France).

Plasmids and transfection

The PRDX3 cDNA (NM_006793) was tagged with Myc-DDK in C-ter and cloned in pCMV6 (Origene Technologies, Inc., Rockville, MD, USA). Oligonucleotide primers containing *Hind*III and *Bam*HI sites (Supplementary Material, Table S1) were designed for polymerase chain reaction (PCR)-based subcloning of PRDX3 and Myc-DDK tags into the pcDNA3.1 expression vector (Invitrogen, Carlsbad, CA, USA).

The PRDX3 p.D163E, p.D202N and p.A142G mutations were generated with specific primers (Supplementary Material, Table S1) using the QuikChange Site-Directed Mutagenesis Kit (Agilent, Santa Clara, CA, USA). WT and p.D163E-PRDX3 sequences were further subcloned at *Eco*RI and *Xho*I sites into the bicistronic pCAGIG plasmid. pCAGIG empty vector was assembled by Dr Matsuda and kindly provided by Dr Flames (54,55).

HeLa cells were transiently transfected for 24 h with 1 μg of WT or mutated PRDX3 plasmids and FuGENE HD Transfection Reagent (Promega, Madison, WI, USA).

WB analysis

To obtain the total cellular extracts, fibroblasts or transiently transfected HeLa cells were washed once, scraped with phosphate-buffered saline (PBS) and centrifuged. Cell pellets were lysed with RIPA buffer (Sigma-Aldrich) containing a protease inhibitor cocktail (Roche Diagnostics GmbH, Mannheim, Germany) for 30 min before centrifugation (15 000 g, 15 min, 4°C). Protein concentration of the supernatant (RIPA-soluble protein fraction) was quantified using the BCA (bicinchoninic acid) method (Thermo Fisher Scientific, Waltham, MA, USA), and a final amount of 20 μg was employed for WB analysis. The insoluble fraction was washed once with lysis buffer and the pellet obtained after a second centrifugation was lysed in Laemmli buffer 4× (Bio-Rad Laboratories, Inc., Hercules, CA, USA) containing 2-mercaptoethanol, boiled with shaking for 15 min, and finally analyzed by WB.

Samples were loaded on a 12.5% polyacrylamide gel under reducing conditions. Polyvinylidene fluoride membranes were blocked with 5% milk powder in tris-buffered saline with tween and incubated overnight at 4°C with primary antibodies. The following day, the membranes were incubated with the appropriate

secondary horseradish peroxidase–conjugated antibodies (Invitrogen). Immunoreactive protein bands were visualized using enhanced chemiluminescence plus reagent (Thermo Fisher Scientific). Primary antibody dilutions used in WB were as follows: anti-FLAG M2® (F3165, Sigma-Aldrich): 1/3000; anti-α-tubulin (T8203, Santa Cruz Biotechnology, Dallas, TX, USA): 1/3000; anti-PRDX3 (PA1835, Boster Biological Technology, Pleasanton, CA, USA): 1/1000 and anti-p62 (sc-28 359, Santa Cruz Biotechnology): 1/1000.

Proteasomal and autophagic degradation assays

HeLa cells, after 24 h transfection with WT or D163E constructs, were treated with 30 μM MG-132 (Abcam, Cambridge, UK) to test for proteasomal degradation of PRDX3 or 200 nM bafilomycin A1 (Santa Cruz Biotechnology) to evaluate the lysosomal degradation pathway, and DMSO as vehicle control. After 24 h incubation, the cells were harvested and analyzed by WB as described earlier.

Immunofluorescence assays in HeLa cells and fibroblasts

HeLa cells transfected with WT or mutated forms of PRDX3 were stained *in vivo* with 100 nM Mitotracker® Red CMXRos (Invitrogen) during 30 min at 37°C, 5% CO_2 and darkness. Then, the cells were washed three times with PBS at 37°C and fixed in 4% paraformaldehyde. After permeabilization with 0.25% Triton X-100/PBS, the cells were blocked and immunostained with anti-FLAG M2 antibody (1/500; F3165, Sigma-Aldrich) in 5% horse-serum/PBS. The following day, they were exposed to the appropriate secondary antibodies conjugated with fluorophores Alexa FluorTM (Invitrogen) for 1 h at room temperature. Coverslips containing stained cells were assembled with Vecta-Shield Mounting Medium containing 4′,6-diamidino-2-phenylindole (DAPI; Vector Laboratories, Burlingame, CA, USA). For primary fibroblasts culture, the same protocol was followed, except for the fact that the primary antibody was anti-PRDX3 (1/500; PA1835, Boster Biological Technology). The slides were examined using the SP8-Leica confocal microscope (Leica Microsystems, Wetzlar, Germany). To assess mitochondrial morphology in transfected HeLa cells, images were captured with identical confocal settings for all genotypes and experimental replicates using a 63× oil immersion objective.

Evaluation of mitochondrial superoxide status

The level of mitochondrial superoxide anion in fibroblasts was assessed in basal growing conditions and after exposure to 50 μM H_2O_2, using ROS-sensitive fluorescent probe MitoSox™ Red (Molecular Probes, Eugene, OR, USA). Fibroblasts were seeded in six-well plates (100 000 cells/well) for 48 h and treated with H_2O_2 for two additional hours. Subsequently, cells were harvested, washed and incubated for 10 min at 37°C and 5% CO_2 in the presence of 4 μM MitoSox™ Red in PBS 1× and immediately analyzed in a CytoFLEX S flow cytometer (Beckman Coulter, Inc., Brea, CA, USA) after addition of the viability dye DAPI (Sigma-Aldrich) at a concentration of 1 μg/ml. MitoSox™ Red fluorescence was excited with a 561 nm laser line and a phycoerythrin filter (585/42 nm) was used to detect the emission. The mean fluorescence intensity (MFI) of 10 000 cells per sample was measured and corrected for autofluorescence from unlabeled cells. Experiments were performed in triplicate and repeated at least three times. Each sample was normalized to the untreated control fibroblasts to yield the normalized MFI.

MTS assay

Cell viability was evaluated in control- and patient-derived fibroblasts using the MTS Assay Kit (Abcam) in basal growing conditions and after exposure to H_2O_2 (50, 100 μM) for 2 h or L-BSO (3, 6, 10, 50 μM) for 16 h (Sigma-Aldrich). Fibroblasts were seeded in triplicates in 96-well plates at a density of 7500 or 10 000 cells/well, and cultured in DMEM high-glucose medium for 16 h. After incubation with H_2O_2 or L-BSO, the medium was replaced, and 20 μl of MTS tetrazolium was added to each well (darkness, 4 h, 37°C). Reduction of the MTS tetrazolium compound by viable mammalian cells generates formazan dye, which was quantified by measuring the absorbance at 490 nm in a spectrophotometer (Perkin-Elmer, Inc., Waltham, MA, USA). Optical density (OD) values were normalized to those of the untreated control and three independent experiments were performed.

Quantitative PCR analysis

Total RNA was extracted from cultured fibroblast using RNeasy Mini Kit (Qiagen, Hilden, Germany) and cDNA was synthesized with qScript cDNA SuperMix (Quantabio, Beverly, MA, USA) from 1.0 μg of total RNA. For the reaction, 2 μl of a 1/8 cDNA dilution with the appropriate volume of LightCycler® 480 SYBR® (Roche Molecular Diagnostics, Pleasanton, CA, USA) and the primers (Supplementary Material, Table S1) were mixed and incubated in a LightCycler® 480 System thermocycler (Roche Molecular Diagnostics). The expression level of targets was normalized to *GAPDH* levels and $2^{-\Delta\Delta CT}$ method was used for relative quantification. Three biological replicates and three quantitative PCR (qPCR) reactions were done for each condition.

Mitochondrial morphology

To estimate the cell percentage according to mitochondrial morphology (aggregated, fragmented, tubular or intermediate) and quantitative mitochondrial morphological parameters, we used HeLa cells overexpressing PRDX3-WT and the missense mutations p.D163E detected in our patient and p.D202N and p.A142G previously reported (7). Living cells were stained with Mitotracker® Red CMXRos and anti-FLAG M2® as described above, and images were captured on a Leica SP8 confocal microscope (Leica Microsystems) with identical confocal settings for all genotypes and

experimental replicates using a 63× oil immersion objective. For each experimental group, at least 120 PRDX3-FLAG-expressing cells from three independent experiments were analyzed.

Quantitative analysis of mitochondrial network morphology was carried out using ImageJ™ approaches: Mito-Morphology macro and Mitochondrial Network Analysis (MiNA) (20,21,56). The macro calculates the mitochondria's number, circularity, perimeter (μm), area (μm^2), and the percentage of cell area occupied by mitochondria. Index of elongation (inverse of circularity) is validated as a mitochondrial fission parameter and interconnectivity (area/perimeter ratio) as a mitochondrial fusion parameter. MiNA was used to evaluate the extent of mitochondrial branches, and mitochondrial footprint (area occupied by mitochondrial structures in the cell).

Electron microscopy

For CLEM studies HeLa cells were seeded in a permanox Lab-Tek chamber slide of 8 wells (Nalge Nunc International, Naperville, IL, USA) at a density of 10 000 cells/well and transfected for 24 h with the plasmid p.CDNA_PRDX3 D163E tagged with Myc-DDK. Then, cells were fixed and immunostained with anti- FLAG M2 as mentioned above, except for the permeabilization step that was suppressed. The slides were assembled with Vecta-Shield Mounting Medium containing DAPI. The confocal images were acquired with a Leica TCS SP8 HyVolution II (Leica Microsystems) inverted laser scanning confocal microscope using oil objective 63× Plan-Apochromat-Lambda Blue 1.4 N.A. The excitation wavelengths for fluorochromes were 488 nm for Alexa 488 and 405 nm for DAPI. Two-dimensional pseudo color images (255 color levels) were gathered with a size of 1024 × 1024 pixels and Airy 1 pinhole diameter. After fluorescence capture, slides were processed for transmission electron microscopy (TEM) analysis.

The samples were post-fixed in 2% OsO4 for 1 h at room temperature and stained in 2% uranyl acetate in the dark (2 h, 4°C). Then, were rinsed in distilled water, dehydrated in ethanol and infiltrated overnight in durcupan resin (Sigma-Aldrich). Following polymerization, embedded cultures were detached from the wells and glued to durcupan blocks. Finally, ultra-thin sections (0.08 μm) were cut with an Ultracut UC-6 (Leica Microsystems), stained with lead citrate (Reynolds solution) and examined under a transmission electron microscope FEI Tecnai Spirit BioTwin (Thermo Fisher Scientific). Pictures were taken using Radius software v2.1 with a Xarosa digital camera (EMSIS GmbH, Münster, Germany). Six HeLa cells expressing PRDX3 p.D163E and four non-transfected cells were analyzed.

A final overlay of the TEM and fluorescence images was performed in ICY (Open Source Image Processing Software), using eC-CLEM plug-in for imaging correlation (57).

Primary neuronal cultures

Primary cultures of cortical neurons were prepared from embryonic day 15 (E15.5) CD1 mice, as previously described (18). Cortices were washed with Hank's solution, dissociated by mechanical disaggregation in 5 ml of plating medium (minimum essential medium supplemented with 10% horse serum and 20% glucose), plated into pre-coated dishes with poly L-lysine (Sigma-Aldrich) (150 000 cells per well in 12-well plates) and placed into a humidified incubator containing 95% air and 5% CO_2. After 2 h of incubation, the plating medium was replaced with equilibrated neurobasal media supplemented with B27 and GlutaMAX (Gibco, Thermo Fisher Scientific).

Neuronal transfection and mitochondrial staining

The primary neurons were transfected at D4 with Lipofectamine 2000 (Thermo Fisher Scientific), according to the manufacturer's instructions, with pCAGIG plasmids expressing either WT-PRDX3 or PRDX3 p.D163E. Upon transfection, mitochondria of transfected primary neurons at D5 and D12 were stained with MitoTracker® Red CMXRos (Thermo Fisher Scientific) according to the manufacturer's protocol. Primary neurons were incubated with MitoTracker® Red CMXRos (100 nM) for 20 min in dark (37°C, 5% CO_2).

Neuronal cell immunofluorescence assays

Neurons were fixed with 4% paraformaldehyde and immunofluorescence was carried out according to standard protocols, permeabilizing with PBS with 0.1% Triton and blocking with 2% PBS-BSA (bovine serum albumin). Primary and secondary antibodies were diluted in 2% PBS-BSA: anti-GFP (1/500; GFP-1010, Aves Labs, David, CA, USA), anti-PRDX3 (1/350; PA1835, Boster Biological Technology), goat anti-chicken AlexaFluor® 488 (1/500; A-11039, Thermo Fisher Scientific) and donkey anti-rabbit AlexaFluor® 647 (1/500; A-31573, Life Technologies, Carlsbad, CA, USA). After staining, the coverslips were mounted in mowiol for imaging.

For intensity and colocalization analyses, pictures were taken with a Leica Dmi8 microscope with 20X/0.3 NA Plan-Neofluar or 63X Plan-Apochromat/1.4 NA objectives. For the neurite damage analysis, fields of 3×3 photos were taken with a Zeiss Observer Z1 microscope with an AxioCam MRm (16 pixels) and Apotome 2 incorporated and 20× LD A-plan 0.5 NA objective.

Colocalization and intensity analyses were performed with ImageJ. All the pictures were equally processed and analyzed in three different regions: soma, proximal neurite (0–15 μm from soma) and distal neurite (15–30 μm from soma). The colocalization analysis was performed with the JACoP plugin, considering Pearson's correlation coefficient and Manders' M1 and M2 coefficients. Finally, for neurite damage analysis, the status of the biggest neurite was analyzed in each neuron in a radius of

150 μm from the soma and classified as an intact neurite or a neurite with swelling or degeneration.

Statistical analysis

Data were analyzed using GraphPad Prism 6.0 software (GraphPad Software, Inc., San Diego, CA, USA), and all results were expressed as mean ± standard error of the mean (SEM) or standard deviation (SD), as indicated in the figure legends. For normally distributed data, when comparing two groups, the analysis was conducted via unpaired *t*-tests. Statistical analysis of three or more groups was performed by one-way ANOVA followed by Dunnett's test compared to WT genotype (WB) or followed Tukey's test (mitochondrial morphology).

Supplementary Material

Supplementary Material is available at *HMG* online.

Acknowledgements

We would like to thank the patient and his family for agreeing to participate in this study. We are grateful to Dr David Pla-Martín for critically reading of the manuscript.

Conflict of Interest statement. The authors declare that they have no conflict of interest.

Funding

The Instituto de Salud Carlos III (ISCIII)—Subdirección General de Evaluación y Fomento de la Investigación within the framework of the National R + D + I Plan co-funded with European Regional Development Funds (ERDF) (grants PI18/00147 and PI21/00103 to C.E.); the Spanish Ministry of Economy and Competitiveness (grant SAF2017-89020-R to P.F.); the Fundació La Marató TV3 (grants 20143130 and 20143131 to B.P.-D. and C.E.) and the Generalitat Valenciana (grant PROMETEO/2018/135 to C.E.). Part of the equipment employed in this work was funded by Generalitat Valenciana and co-financed with ERDF (OP ERDF of Comunitat Valenciana 2014-2020). P.F. and A.R.-P. are supported by the Spanish Ministry of Science and Innovation (grants RyC-2014-16410 to P.F. and PRE2018-083562 to A.R.-P.).

References

1. Mattson, M.P., Gleichmann, M. and Cheng, A. (2008) Mitochondria in neuroplasticity and neurological disorders. *Neuron*, **60**, 748–766.
2. Zhou, B., Lin, M.Y., Sun, T., Knight, A.L. and Sheng, Z.H. (2014) Characterization of mitochondrial transport in neurons. *Methods Enzymol.*, **547**, 75–96.
3. Hinarejos, I., Machuca-Arellano, C., Sancho, P. and Espinos, C. (2020) Mitochondrial dysfunction, oxidative stress and neuroinflammation in neurodegeneration with brain iron accumulation (NBIA). *Antioxidants (Basel)*, **9**, 1020.
4. Singh, A., Kukreti, R., Saso, L. and Kukreti, S. (2019) Oxidative stress: a key modulator in neurodegenerative diseases. *Molecules*, **24**, 1583.
5. Tello, C., Darling, A., Lupo, V., Pérez-Dueñas, B. and Espinós, C. (2018) On the complexity of clinical and molecular bases of neurodegeneration with brain iron accumulation. *Clin. Genet.*, **93**, 731–740.
6. Holzerova, E., Danhauser, K., Haack, T.B., Kremer, L.S., Melcher, M., Ingold, I., Kobayashi, S., Terrile, C., Wolf, P., Schaper, J. *et al.* (2016) Human thioredoxin 2 deficiency impairs mitochondrial redox homeostasis and causes early-onset neurodegeneration. *Brain*, **139**, 346–354.
7. Rebelo, A.P., Eidhof, I., Cintra, V.P., Guillot-Noel, L., Pereira, C.V., Timmann, D., Traschutz, A., Schols, L., Coarelli, G., Durr, A. *et al.* (2021) Biallelic loss-of-function variations in PRDX3 cause cerebellar ataxia. *Brain*, **144**, 1467–1481.
8. Renaud, M., Tranchant, C., Martin, J.V.T., Mochel, F., Synofzik, M., van de Warrenburg, B., Pandolfo, M., Koenig, M., Kolb, S.A., Anheim, M. *et al.* (2017) A recessive ataxia diagnosis algorithm for the next generation sequencing era. *Ann. Neurol.*, **82**, 892–899.
9. Baxter, P. (2012) Chapter 36 - Acute ataxia: Epidemiology and Differential Diagnosis. In Schmahmann, E.B.J. (ed), *Cerebellar Disorders in Children*. Mac Keith Press, London.
10. Darling, A., Aguilera-Albesa, S., Tello, C.A., Serrano, M., Tomas, M., Camino-Leon, R., Fernandez-Ramos, J., Jimenez-Escrig, A., Poo, P., O'Callaghan, M. *et al.* (2019) PLA2G6-associated neurodegeneration: new insights into brain abnormalities and disease progression. *Parkinsonism Relat. Disord.*, **61**, 179–186.
11. Sancho, P., Andrés-Bordería, A., Gorría-Redondo, N., Llano, K., Martínez-Rubio, D., Yoldi-Petri, M.E., Blumkin, L., Rodríguez de la Fuente, P., Gil-Ortiz, F., Fernández-Murga, L. *et al.* (2021) Expanding the β-III spectrin-associated phenotypes toward non-progressive congenital ataxias with neurodegeneration. *Int. J. Mol. Sci.*, **22**, 2505.
12. Richards, S., Aziz, N., Bale, S., Bick, D., Das, S., Gastier-Foster, J., Grody, W.W., Hegde, M., Lyon, E., Spector, E. *et al.* (2015) Standards and guidelines for the interpretation of sequence variants: a joint consensus recommendation of the American College of Medical Genetics and Genomics and the Association for Molecular Pathology. *Genet. Med.*, **17**, 405–424.
13. Cox, A.G., Winterbourn, C.C. and Hampton, M.B. (2009) Mitochondrial peroxiredoxin involvement in antioxidant defence and redox signalling. *Biochem. J.*, **425**, 313–325.
14. Zorov, D.B., Juhaszova, M. and Sollott, S.J. (2014) Mitochondrial reactive oxygen species (ROS) and ROS-induced ROS release. *Physiol. Rev.*, **94**, 909–950.
15. Holzerova, E. and Prokisch, H. (2015) Mitochondria: much ado about nothing? How dangerous is reactive oxygen species production? *Int. J. Biochem. Cell Biol.*, **63**, 16–20.
16. Zhang, H., Go, Y.M. and Jones, D.P. (2007) Mitochondrial thioredoxin-2/peroxiredoxin-3 system functions in parallel with mitochondrial GSH system in protection against oxidative stress. *Arch. Biochem. Biophys.*, **465**, 119–126.
17. Fazzari, P., Snellinx, A., Sabanov, V., Ahmed, T., Serneels, L., Gartner, A., Shariati, S.A., Balschun, D. and De Strooper, B. (2014) Cell autonomous regulation of hippocampal circuitry via Aph1b-gamma-secretase/neuregulin 1 signalling. *elife*, **3**, e02196.
18. Navarro-Gonzalez, C., Huerga-Gomez, A. and Fazzari, P. (2019) Nrg1 intracellular signaling is neuroprotective upon stroke. *Oxidative Med. Cell. Longev.*, **2019**, 3930186.
19. Wonsey, D.R., Zeller, K.I. and Dang, C.V. (2002) The c-Myc target gene PRDX3 is required for mitochondrial homeostasis and

neoplastic transformation. *Proc. Natl. Acad. Sci. U. S. A.*, **99**, 6649–6654.
20. Dagda, R.K., Cherra, S.J., 3rd, Kulich, S.M., Tandon, A., Park, D. and Chu, C.T. (2009) Loss of PINK1 function promotes mitophagy through effects on oxidative stress and mitochondrial fission. *J. Biol. Chem.*, **284**, 13843–13855.
21. Valente, A.J., Maddalena, L.A., Robb, E.L., Moradi, F. and Stuart, J.A. (2017) A simple ImageJ macro tool for analyzing mitochondrial network morphology in mammalian cell culture. *Acta Histochem.*, **119**, 315–326.
22. Yewdall, N.A., Venugopal, H., Desfosses, A., Abrishami, V., Yosaatmadja, Y., Hampton, M.B., Gerrard, J.A., Goldstone, D.C., Mitra, A.K. and Radjainia, M. (2016) Structures of human peroxiredoxin 3 suggest self-chaperoning assembly that maintains catalytic state. *Structure*, **24**, 1120–1129.
23. Conchillo-Sole, O., de Groot, N.S., Aviles, F.X., Vendrell, J., Daura, X. and Ventura, S. (2007) AGGRESCAN: a server for the prediction and evaluation of "hot spots" of aggregation in polypeptides. *BMC Bioinformatics*, **8**, 65.
24. Udhaya-Kumar, S., Bithia, R., Thirumal-Kumar, D., Doss, C. G. P. and Zayed, H. (2022) Mutational landscape of K-Ras substitutions at 12th position-a systematic molecular dynamics approach. *J. Biomol. Struct. Dyn.*, **40**, 1571–1585.
25. De Baets, G., Van Durme, J., Reumers, J., Maurer-Stroh, S., Vanhee, P., Dopazo, J., Schymkowitz, J. and Rousseau, F. (2012) SNPeffect 4.0: on-line prediction of molecular and structural effects of protein-coding variants. *Nucleic Acids Res.*, **40**, D935–D939.
26. Lindholm, D., Korhonen, L., Eriksson, O. and Koks, S. (2017) Recent insights into the role of unfolded protein response in ER stress in health and disease. *Front. Cell Dev. Biol.*, **5**, 48.
27. Shpilka, T. and Haynes, C.M. (2018) The mitochondrial UPR: mechanisms, physiological functions and implications in ageing. *Nat. Rev. Mol. Cell Biol.*, **19**, 109–120.
28. Bergmann, T.J., Fregno, I., Fumagalli, F., Rinaldi, A., Bertoni, F., Boersema, P.J., Picotti, P. and Molinari, M. (2018) Chemical stresses fail to mimic the unfolded protein response resulting from luminal load with unfolded polypeptides. *J. Biol. Chem.*, **293**, 5600–5612.
29. Quiles, J.M. and Gustafsson, A.B. (2020) Mitochondrial quality control and cellular Proteostasis: two sides of the same coin. *Front. Physiol.*, **11**, 515.
30. Brunetti, D., Catania, A., Viscomi, C., Deleidi, M., Bindoff, L.A., Ghezzi, D. and Zeviani, M. (2021) Role of PITRM1 in mitochondrial dysfunction and neurodegeneration. *Biomedicine*, **9**, 833.
31. Shiiba, I., Takeda, K., Nagashima, S. and Yanagi, S. (2020) Overview of mitochondrial E3 ubiquitin ligase MITOL/MARCH5 from molecular mechanisms to diseases. *Int. J. Mol. Sci.*, **21**, 3781.
32. de Diego, V., Martinez-Monseny, A.F., Muchart, J., Cuadras, D., Montero, R., Artuch, R., Perez-Cerda, C., Perez, B., Perez-Dueñas, B., Poretti, A. *et al.* (2017) Longitudinal volumetric and 2D assessment of cerebellar atrophy in a large cohort of children with phosphomannomutase deficiency (PMM2-CDG). *J. Inherit. Metab. Dis.*, **40**, 709–713.
33. Serrano, N.L., De Diego, V., Cuadras, D., Martinez Monseny, A.F., Velazquez-Fragua, R., Lopez, L., Felipe, A., Gutierrez-Solana, L.G., Macaya, A., Perez-Duenas, B. *et al.* (2017) A quantitative assessment of the evolution of cerebellar syndrome in children with phosphomannomutase-deficiency (PMM2-CDG). *Orphanet J. Rare Dis.*, **12**, 155.
34. Hattori, F., Murayama, N., Noshita, T. and Oikawa, S. (2003) Mitochondrial peroxiredoxin-3 protects hippocampal neurons from excitotoxic injury in vivo. *J. Neurochem.*, **86**, 860–868.
35. Course, M.M. and Wang, X. (2016) Transporting mitochondria in neurons. *F1000Res*, **5**(F1000 Faculty Rev), 1735. https://doi.org/10.12688/f1000research.7864.1
36. Sancho, P., Bartesaghi, L., Miossec, O., Garcia-Garcia, F., Ramirez-Jimenez, L., Siddell, A., Akesson, E., Hedlund, E., Lassuthova, P., Pascual-Pascual, S.I. *et al.* (2019) Characterization of molecular mechanisms underlying the axonal Charcot-Marie-tooth neuropathy caused by MORC2 mutations. *Hum. Mol. Genet.*, **28**, 1629–1644.
37. Gouttenoire, E.A., Lupo, V., Calpena, E., Bartesaghi, L., Schupfer, F., Medard, J.J., Maurer, F., Beckmann, J.S., Senderek, J., Palau, F. *et al.* (2013) Sh3tc2 deficiency affects neuregulin-1/ErbB signaling. *Glia*, **61**, 1041–1051.
38. Soto, C. and Pritzkow, S. (2018) Protein misfolding, aggregation, and conformational strains in neurodegenerative diseases. *Nat. Neurosci.*, **21**, 1332–1340.
39. Lingor, P., Koch, J.C., Tonges, L. and Bahr, M. (2012) Axonal degeneration as a therapeutic target in the CNS. *Cell Tissue Res.*, **349**, 289–311.
40. Wiemerslage, L. and Lee, D. (2016) Quantification of mitochondrial morphology in neurites of dopaminergic neurons using multiple parameters. *J. Neurosci. Methods*, **262**, 56–65.
41. Liao, Y., Tham, D.K.L., Liang, F.-X., Chang, J., Wei, Y., Putty-Reddy, S., Sall, J., Ren, S.J., Chicote, J.U., Arnold, L.L. *et al.* (2019) Mitochondrial lipid droplet formation as a detoxification mechanism to sequester and degrade excessive urothelial membranes. *Mol. Biol. Cell*, **30**, 2969–2984.
42. Farmer., B. C., Walsh, A. E., Kluemper, J. C. and Johnson, L. A. (2020) Lipid droplets in neurodegenerative disorders. *Front. Neurosci.*, **14**, 742.
43. Geltinger, F., Schartel, L., Wiederstein, M., Tevini, J., Aigner, W., Felder, T.K. and Rinnerthaler, M. (2020) Friend or foe: lipid droplets as organelles for protein and lipid storage in cellular stress response, aging and disease. *Molecules*, **25**, 5053.
44. Bischof, J., Salzmann, M., Streubel, M. K., Hasek, J., Geltinger, F., Duschi, J., Bresgen, N., Briza, P., Haskova, D., Lejskova *et al.* (2017) Clearing the outer mitochondrial membrane from harmful proteins via lipid droplets. *Cell Death Discov.* **3**, 17016.
45. Yewdall, N.A., Peskin, A.V., Hampton, M.B., Goldstone, D.C., Pearce, F.G. and Gerrard, J.A. (2018) Quaternary structure influences the peroxidase activity of peroxiredoxin 3. *Biochem. Biophys. Res. Commun.*, **497**, 558–563.
46. Umemura, M., Kaneko, Y., Tanabe, R. and Takahashi, Y. (2021) ATF5 deficiency causes abnormal cortical development. *Sci. Rep.*, **11**, 7295.
47. Pollecker, K., Sylvester, M. and Voos, W. (2021) Proteomic analysis demonstrates the role of the quality control protease LONP1 in mitochondrial protein aggregation. *J. Biol. Chem.*, **297**, 101134.
48. Wodrich, A.P.K., Scott, A.W., Shukla, A.K., Harris, B.T. and Giniger, E. (2022) The unfolded protein responses in health, aging, and neurodegeneration: recent advances and future considerations. *Front. Mol. Neurosci.*, **15**, 831116.
49. Schmitz-Hubsch, T., du Montcel, S.T., Baliko, L., Berciano, J., Boesch, S., Depondt, C., Giunti, P., Globas, C., Infante, J., Kang, J.S. *et al.* (2006) Scale for the assessment and rating of ataxia: development of a new clinical scale. *Neurology*, **66**, 1717–1720.
50. Correa-Vela, M., Lupo, V., Montpeyo, M., Sancho, P., Marce-Grau, A., Hernandez-Vara, J., Darling, A., Jenkins, A., Fernandez-Rodriguez, S., Tello, C. *et al.* (2020) Impaired proteasome activity and neurodegeneration with brain iron accumulation in FBXO7 defect. *Ann. Clin. Transl. Neurol.*, **7**, 1436–1442.
51. Sánchez-Monteagudo, A., Alvarez-Sauco, M., Sastre, I., Martínez-Torres, I., Lupo, V., Berenguer, M. and Espinós, C. (2020) Genetics

of Wilson disease and Wilson-like phenotype in a clinical series from eastern Spain. *Clin. Genet.*, **97**, 758–763.
52. Fowler, A., Mahamdallie, S., Ruark, E., Seal, S., Ramsay, E., Clarke, M., Uddin, I., Wylie, H., Strydom, A., Lunter, G. *et al.* (2016) Accurate clinical detection of exon copy number variants in a targeted NGS panel using DECoN. *Wellcome Open Res.*, **1**, 20.
53. Krissinel, E. and Henrick, K. (2007) Inference of macromolecular assemblies from crystalline state. *J. Mol. Biol.*, **372**, 774–797.
54. Matsuda, T. and Cepko, C.L. (2004) Electroporation and RNA interference in the rodent retina in vivo and in vitro. *Proc. Natl. Acad. Sci. U. S. A.*, **101**, 16–22.
55. Pla-Martin, D., Calpena, E., Lupo, V., Márquez, C., Rivas, E., Sivera, R., Sevilla, T., Palau, F. and Espinós, C. (2015) Junctophilin-1 is a modifier gene of GDAP1-related Charcot-Marie-tooth disease. *Hum. Mol. Genet.*, **24**, 213–229.
56. Molla, B., Munoz-Lasso, D.C., Riveiro, F., Bolinches-Amorós, A., Pallardo, F.V., Fernandez-Vilata, A., de la Iglesia-Vaya, M., Palau, F. and Gonzalez-Cabo, P. (2017) Reversible axonal dystrophy by calcium modulation in Frataxin-deficient sensory neurons of YG8R mice. *Front. Mol. Neurosci.*, **10**, 264.
57. Paul-Gilloteaux, P., Heiligenstein, X., Belle, M., Domart, M-C., Larijani, B., Collinson, L., Raposo, G. and Salamero, J. (2017) eC-CLEM: flexible multidimensional registration software for correlative microscopies. *Nat. Methods*, **14**, 102–103.